J Mater Sci (2014) 49:580–591
DOI 10.1007/s10853-013-7738-2

Phenol formaldehyde adhesives formulated for advanced X-ray imaging in wood-composite bondlines

Jesse L. Paris · Frederick A. Kamke · Reginald Mbachu · Sara Kraushaar Gibson

Received: 9 July 2013 / Accepted: 12 September 2013 / Published online: 26 September 2013
© Springer Science+Business Media New York 2013

Abstract A phenol formaldehyde (PF) adhesive was uniformly tagged with iodine such that it yielded sufficient X-ray computed tomography (XCT) gray-scale contrast for material segmentation in reconstructed wood-composite bondlines. Typically, untagged adhesives are organic and have a similar solid-state density as wood cell-walls, and therefore cannot be segmented quantitatively in XCT data. The iodinated PF development involved analysis and comparison of three trial adhesives containing rubidium, bromine, or iodine. Adhesive tag efficacy was measured in terms of X-ray absorption contrast enhancement and tag uniformity along the adhesive polymers. Cured adhesive density, tag element, and concentration were each found to significantly impact XCT contrast results, which in turn agreed with theoretical X-ray attenuation predictions for each resin. Ion chromatography confirmed the absence of free iodide in the liquid PF prior to bonding, and fluorescence microscopy and energy-dispersive spectroscopy (EDS) showed that iodine tags remained associated with the cured adhesive polymers. XCT and EDS results also demonstrated that when contrast agents are simply mixed into resins, rather than attached to the polymer chains, they are free to migrate independent of the penetrating adhesives during bonding. This then can cause complications with quantitative segmentation and analyses. The iodinated PF yielded consistent and uniform XCT gray-scale contrast; its formulation could be adjusted for other viscosity or molecular weight distribution, which would affect its penetration behavior.

J. L. Paris (✉) · F. A. Kamke (✉)
Department of Wood Science and Engineering, and the Wood-Based Composites Center, Oregon State University, 119 Richardson Hall, Corvallis, OR 97331, USA
e-mail: jesse.paris@oregonstate.edu

F. A. Kamke
e-mail: fred.kamke@oregonstate.edu

R. Mbachu · S. K. Gibson
Arclin Chemical, 475 28th St., Springfield, OR 97477, USA

Introduction

Reducing solid wood into smaller components and reforming them into engineered composite materials via adhesive bonding extends the resource and randomizes natural variation affording composites more uniform material properties [1]. Adhesive penetration and subsequent solidification in the porous wood structures increase the surface area over which the intermolecular chemical interactions governing wood adhesion effectively operate, and mechanically interlock the adherends [2]. Additionally, penetration transfers joint-stresses, past inherent surface irregularities, and machining defects, into undamaged wood cells which is believed to enhance bond strength, toughness, and durability [1, 3–5]. However, debate remains as to the quantitative role of adhesive penetration, and what is considered an optimum or sufficient level, in composite joint assemblies. These issues are difficult to ascertain, in part, because adhesive penetration is commonly assessed with various two-dimensional (2D) microscopy techniques which are both destructive to the composite specimen and neglect the true three-dimensional (3D) bond [6].

X-ray computed tomography (XCT) is non-destructive and provides 3D images for the internal structures of materials. XCT is an extremely valuable analytical tool in medical, mechanical engineering, and materials-science research disciplines, and within the past decade has grown in application to wood and wood-composites [7–16]. While

XCT has yielded detailed micro-scale 3D wood anatomy data [12, 14, 17–20], tracking adhesive infiltration has proven difficult with typical adsorption contrast tomography.

Absorption contrast is achieved when neighboring materials have different linear attenuation coefficients, μ. This value relates to the mean free path of a penetrating X-ray photon in a material before being absorbed or scattered. With highly coherent, mono-energetic X-ray photons, as is the case with synchrotron radiation sources, μ is easily calculated according to Beer–Lambert's law as the ratio of the transmitted, I, to initial, I_0, radiation intensity through the material's thickness, d [21, 22].

$$I/I_0 = \exp^{(-\mu d)}$$

The value of the linear attenuation coefficient is a function of both the material's elemental composition and density; dense materials and those with high atomic number (Z) contain more electrons per unit volume, and thus have higher μ values [7]. Wood and phenol formaldehyde (PF) adhesives are both organic, being primarily composed of carbon, hydrogen, and oxygen; moreover, once cured, the PF density is similar to that of the wood cell-wall at approximately 1.5 g/cm^3. Therefore, wood-composite XCT reconstructions often show minimal gray-scale intensity differences between the wood and adhesive phases at micron-scale resolutions, which makes quantitative material segmentation nearly impossible [11, 15]. Several researchers have attempted to overcome these problems by tagging the adhesive, or matrix phase in the case of wood–plastic composites, with various heavy metal contrast agents [9, 13, 15, 16, 23, 24]; however, two significant complications have been identified from these tagging methods. First, phase separation and tag mobility are suspected. If tag compounds are not directly attached to the adhesive pre-polymers, they are free to migrate [11, 15]. Such tag mobility can result in agglomeration, and thus differences in localized attenuation values within the resin phase [13, 23, 24]. Second, if tags do remain associated with the adhesive phase, it is often unclear how uniform they are distributed along the polymer chains. PF adhesives are typically poly-disperse systems with complex reaction schemes during formulation; one would not expect long and short polymer chains to be tagged to the same degree. This too might cause variations in adhesive attenuation coefficients, as resin mobility and penetration depth are, in part, a function of molecular weight. Both complications reduce confidence and accuracy when segmenting wood-composite micro-XCT data into the three distinct material phases: air in the lumens, wood cell-wall, and cured adhesive. This paper demonstrates a method for homogeneously tagging a resol, PF adhesive with iodine (I) to yield sufficient XCT contrast for quantitative material segmentation, with minimal phase overlap. Segmented bondlines can yield novel and valuable 3D information about adhesive penetration within porous wood structures without damaging specimen joints. Method refinement and development involved the formulation and analysis of two preliminary PF resins, partially tagged with bromine (Br) and I.

Experimental

Adhesive formulation

Brominated (BrPF), iodinated (IPF1 and IPF2), and control PF resins (1000–2000 g) were prepared with assistance from Arclin, Springfield, Oregon to mimic conventional plywood resins. *Meta*-bromophenol and *meta*-iodophenol (98 % purity) were included in the BrPF and IPF1 resins at phenol to X-phenol molar ratios of 14.3 and 5.0, respectively; *meta*-iodophenol accounted for the entire phenol component in IPF2. Formulations were prepared with formaldehyde to phenol component molar ratios between 1.8 and 2.5 in the presence of a sodium hydroxide (NaOH) catalyst. Reaction temperatures were controlled between 40 and 90 °C over an 8-h period; formulations were considered complete when resin viscosities were between 500 and 600 mPa s at 25 °C. The final adhesives (43 % solids, pH ~11.5–12.5) were kept frozen (−10 °C) between analyses and bonding.

Gel permeation and ion chromatography

Gel permeation and ion chromatography (GPC and IC, respectively) analyses were conducted by Arclin according to their proprietary analytical procedures. GPC with a Viscotek Triple Detection SEC System and a bank of PLgel columns provided the absolute molecular weight and polydispersity of adhesive. Analysis for bromide and iodide anions was accomplished with a HP1090 instrument equipped with a Shodex CD-4 detector and Hamilton PRP-100X column.

Powder density, neutron activation analysis, and X-ray radiography

Cured resin samples (1–3 g, 125 °C, 3 h) were weighed for percent solids [25], and ground to a powder in a Wiley Mill (30 mesh, ≤0.595 mm). Powder densities were determined according to a modified version of ASTM D 5965, method A [26], where the immersion liquid was deionized water.

Br and I concentrations were verified from cured adhesive powder with neutron activation analysis (NAA). BrPF and IPF1 samples (300–400 mg) were analyzed with epithermal neutrons at the McMaster Nuclear Reactor in

Hamilton, ON, Canada, and induced radioactivity (^{80}Br—617 keV or ^{128}I—443 keV) was collected with a hyper-pure gamma-ray spectrometer. IPF2 samples (100 mg, $n = 3$) were analyzed with thermal neutrons using the TRIGA Mk. II Research Reactor at Oregon State University (OSU), Corvallis, Oregon; subsequent gamma radiation (^{128}I—526.6 keV) was collected with a HPGe detector. Calibration at both facilities was achieved using appropriate sub-standards [27].

Adhesive X-ray adsorption contrast was observed as a function of iodine concentration with ground resin mixtures of IPF1 and a PF control. Polyethylene vials (20 mm tall × 9.5 mm diameter) were partially filled with the homogenized powder mixtures, which were tamped down to minimize void-space. Transmission, 2D radiographs of each vial were collected with polychromatic X-rays (25 kVp, 312 μA) on a cone-beam scanner in the School of Mechanical, Industrial and Manufacturing Engineering at OSU. The system consisted of a Feinfocus 160 kVp source and tungsten target, with a 9-inch image intensifier detector (Medelex HXS-93/PS). Digital gray-scale images were recorded with a 16-bit CCD camera (Point Grey, GRAS-5055 M). A flat-field correction was applied to each radiograph using bright-field and dark-field projections [10]. Image processing and analyses were performed with the software package Fiji, which is based on ImageJ [28, 29]. "Flattened" projections were cropped to a 2-mm-wide vertical column in the center of each vial. Mean gray-scale (transmitted intensity) values were compared for the largest possible areas of both pure air and pure resin powder within each column.

Composite specimen preparation

Single-bondline composite laminates were prepared from Douglas fir (*Pseudotsuga menziesii,* DF), loblolly pine (*Pinus taeda*, SYP), or hybrid poplar (*Populus deltoides* × *Populus trichocarpa*, HP). Individual laminae were conditioned to approximately 12 % moisture content and freshly planed immediately prior to bonding. Adhesives were applied to laminae tangential–longitudinal planes with a steel roller at 120 g/m^2 based on resin solids, and bonded in a hot press (185 °C, 8 min, 689.5 kPa). Specimens (2 mm × 2 mm cross section × 10 mm long) were carefully excised from each laminate using a bandsaw and razor-blade, such that they contained a central, longitudinal bondline.

Fluorescence and scanning electron microscopy (FM and SEM, respectively) and energy-dispersive spectroscopy (EDS)

Composite specimens were embedded with Spurr Low-Viscosity ERL 4221 epoxy under a low vacuum [30, 31] for easier surface preparation and to minimize charge build-up in empty cell lumens during SEM analysis. Ultra-smooth, cross section surfaces were prepared with a Leica EM UC7 ultra microtome, and observed with a Nikon E400 epi-fluorescent microscope, equipped with a high-pressure mercury lamp (100 W) and UV (300–380 nm excitation "EX," 400 nm dichromatic mirror "DM," and 420 nm emission "EM") or blue-light (420–490 nm EX, 500 nm DM and 515 nm EM) filter sets [6, 32]. Digital FM images were collected with a QImaging MicroPublisher 5.0 RTV CCD camera and QCapture Pro 5.1 image software. The same specimen surfaces were subsequently imaged on a FEI Quanta 3D SEM equipped with EDS after being sputter-coated with a thin, conductive layer of a gold/palladium alloy. Elemental maps of carbon, oxygen, nitrogen, sodium, bromine, rubidium, iodine, chlorine, gold, and palladium were collected over the same field of view as the FM images with the following parameters: image resolution 512 × 442 pixels, 16–32 nA beam current, 10–15 kV beam energy, 10.5 mm working distance, 64 frames per map, 200 μs dwell time, and 20–30 % dead time, which resulted in approximately 10–20 K counts/s. Semi-quantitative EDS spectra (100 s) were also collected with the same instrumental parameters from two surface points on each specimen: an adhesive-filled lumen and a cell-wall not in contact with PF resin. Composite (overlaid) elemental maps of oxygen, and the tag element of interest (Br, I, Na, or Rb), were prepared with the following processes in Fiji: (1) single element maps were converted from 8-bit color to grayscale images; (2) high-intensity outlier pixels were removed with a 1-pixel radius; (3) mean "background" pixel values were subtracted from all image points to remove low-intensity (noise); (4) resulting images were linearly normalized, with 0.4 % saturation tolerance, to stretch the pixel intensities over the full 0–255 gray-scale range; and (5) elemental maps were merged to form RGB composites, with the red and green color channels assigned to the oxygen and tag signals, respectively.

Synchrotron, micro X-ray computed tomography (XCT)

XCT analyses were performed at two synchrotron bend-magnet facilities. BrPF and IPF2 composites were scanned on beamline 2-BM-B at the Advanced Photon Source (APS) at the Argonne National Laboratory, Argonne, IL, USA. IPF1 specimens were imaged on beamline 8.3.2 at the Advanced Light Source (ALS) at Lawrence Berkeley National Laboratory, Berkeley, CA, USA. Experimental parameters are provided in Table 1. Both facilities used parallel Si(111) monochromators to image at the specified energies, and LuAG scintillator materials to convert detection signals into visible light. Radiograph projections

Table 1 XCT acquisition parameters for tagged-PF wood-composites

Resin	Beamline	Beam energy (KeV)	Rotation angle (°)	Projections	Exposure time (ms)	Sample to detector distance (mm)	Voxel side length (μm)	Reconstructed slices
Control and BrPF	APS 2-BM-B	14.05	0.12	1504	250	15	1.45	2047
IPF1	ALS 8.3.2	35	0.125	1441	3500	30	0.9	2569
IPF2	APS 2-BM-B	15.3	0.12	1504	250	8	1.45	2047

were then recorded with a 12-bit Roper Scientific CoolSnap K4 HQ CCD camera with 5× objective at the APS, and a 14-bit Cook PCO4000 CCD camera with 10× objective at the ALS. Tomograms from both sources were reconstructed with fast filtered back projection algorithms [10, 33] and stored as stacks of floating point gray-scale slices.

Results and discussion

The three systems discussed in this work, BrPF, IPF1, and IPF2, illustrate the experimental progression undertaken to develop a PF adhesive capable of yielding high gray-scale contrast in micro-XCT images of bonded wood-composites. For comparative purposes, information is also provided for a PF adhesive containing rubidium (Rb), which was studied by Modzel and colleagues in 2009, hereafter referred to as RbPF. The RbPF adhesive did provide significantly enhanced micro-XCT contrast to wood cell-walls [15, 34]; however, the Rb was added as a RbOH catalyst in the PF formulation, in substitute of the more conventional catalyst, NaOH. Having not been directly bound to the PF polymer chains, Rb ions migrated independent of the adhesive penetration during bonding. This migration was proposed to have caused variations in localized Rb concentrations across composite joints, which helped explain contrast differences observed between specimens prepared and scanned under similar conditions [34].

In the present work, it was paramount to develop a system in which the tag element was attached to the resin polymers. Yet, it is important to clarify that the adhesives presented here were not intended to represent the bonding behavior and properties of any particular commercially relevant system. It was recognized that inclusion of contrast agents, of any type or concentration, would undoubtedly influence adhesive properties, which already vary widely across different PF formulations [35, 36]. The primary goal was to prepare a PF system which penetrated the wood upon bonding, transferred bondline stresses once cured, and could be successfully segmented in reconstructed XCT datasets; nevertheless, the presented systems were prepared based on conventional plywood resin formulations in terms of the desired percent solids and viscosity. While BrPF, IPF1, and IPF2 results are all provided together, note that the development of these systems included three separate experiments at synchrotron XCT sites (Table 1), with increasing success in tag efficacy and afforded image contrast. Figure 1 provides example XCT cross section images of composite specimens bonded with each experimental adhesive; in each case, two sub-areas from the same reconstructed slice are provided with their corresponding gray-scale histograms. The first area shows only wood cells and empty lumens, while the second shows the bondline region with adhesive-filled or -coated lumens. Comparison of the histogram shapes within and between each specimen helps illustrate both the adhesive development and some of the image noise and artifacts encountered and overcame throughout this study.

Initially, Br was chosen as the tag element because it has atomic mass similar to Rb ($Z_{Br} = 35$, $Z_{Rb} = 37$), and *meta*-bromophenol has been previously shown to support PF polymerization [37, 38]. During the synthesis of PF resins, methylolation of phenol typically occurs at the *ortho*- and *para*-positions of the ring. The attachment of bromine at the *meta*-position of the ring was not expected to prevent polymerization. The polymerization reaction progressed as expected; however, BrPF failed to yield any noticeable X-ray absorption contrast in the bonded specimens (Fig. 1c, bottom). APS beamline scientists suggested that iodine might be a more effective contrast agent, as it is significantly heavier than bromine ($Z_I = 53$). Thus, IPF1 was prepared using *meta*-iodophenol and at a higher molar ratio to unsubstituted phenol, effectively increasing the tag mass and concentration from the BrPF resin. Yet, IPF1 XCT data suffered from increased image noise, and yielded limited and inconsistent contrast between the wood and adhesive phases. Moreover, in a few instances, the adhesive occupying lumens far from the bondline appeared brighter than the adhesive directly at the joint interface (Fig. 1d, bondline). It was suspected that during formulation the phenol and I-tagged phenol reactants likely polymerized at different

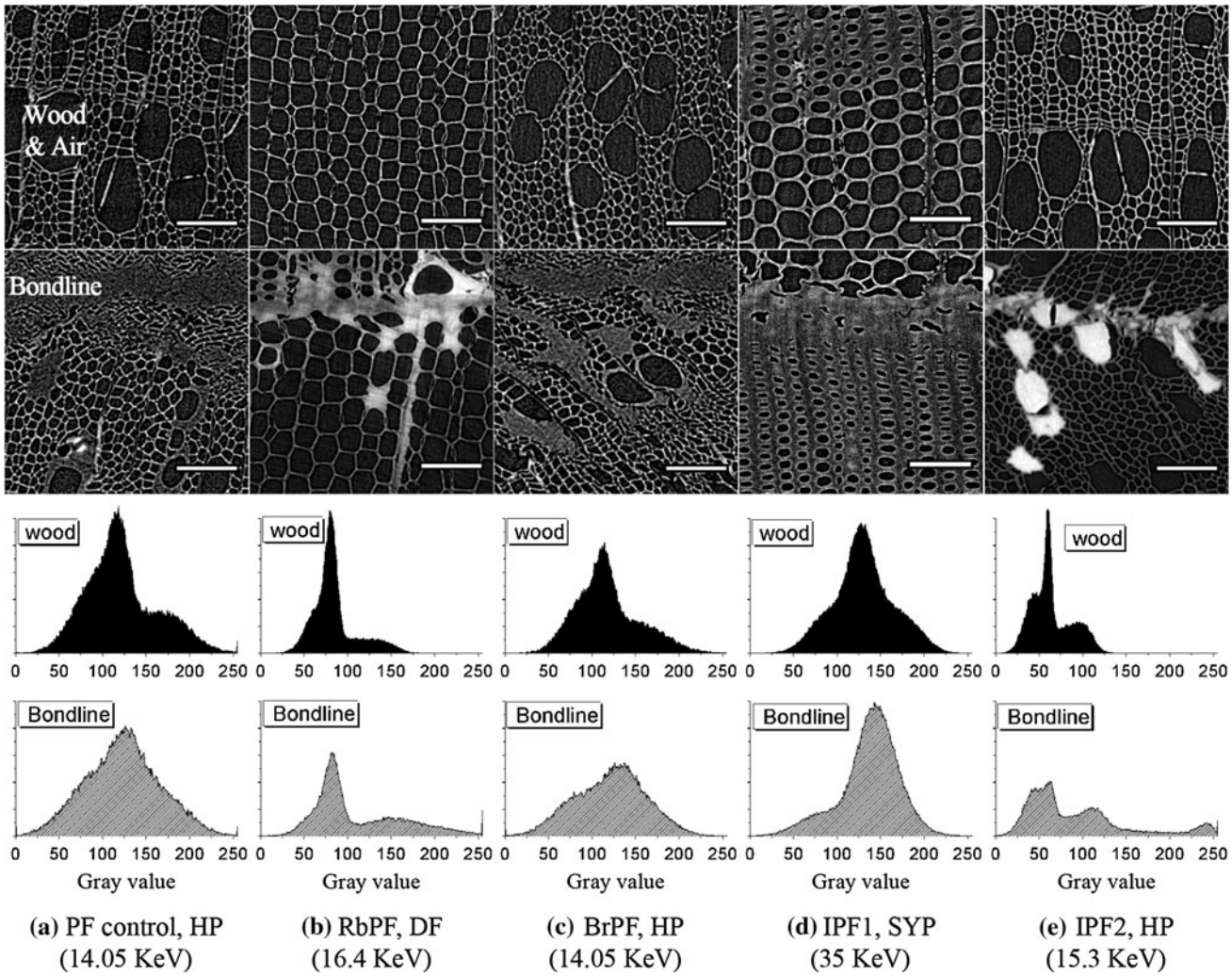

Fig. 1 Cross section XCT slices of each specimen type with indicated scan energy. Sub-areas of wood and air only (*top row*), and region containing a horizontal bondline (*bottom row*) were selected from the same reconstructed image (*scale bars* = 100 μm). Parent images were first normalized to utilize the full 256-bit gray-scale range. *Gray-scale histograms* correspond to the respective sub-areas, and each histogram pair has the same area *under* the *curve* (vertical axis = pixel count)

rates were incorporated into different chain lengths, and perhaps yielded different degrees of branching and cross-linking. Certainly, one would expect the mobility and reactivity of a halogen-substituted phenol to be different relative to an unsubstituted phenol. Consequently, Br and I distributions on the PF adhesive chains were likely heterogeneous, which resulted in different localized tag concentrations in bonded joints. The third adhesive, IPF2, was formulated entirely with *meta*-iodophenol to ensure uniform iodine distribution across all PF polymers, independent of molecular weight or morphology. This also significantly raised the overall wt% I in the cured resin. IPF2 did provide sufficient XCT image contrast for 3D-material segmentation, as depicted in Fig. 2. This paper details the properties of each resin, and why IPF2 was successful compared to the first two trials.

Adhesive properties

Table 2 provides the collective physical properties and tag concentrations for each experimental PF adhesive. Viscosity and molecular weight were measured just after formulation, while density and percent solids were measured from cured samples of each adhesive, with the exception of RbPF; its percent solids, molecular weight, and viscosity were reported elsewhere [34]. The RbPF density of 1.3 g/cm^3 was assigned as a conservative estimate, which neglected any added Rb mass, but was in the typical range of cured PF adhesives [36, 39]. Tag concentrations were first predicted for each adhesive using the percent solids value and known formulation reactant quantities [34], and then measured directly with NAA. Each system resulted in similar solids content and viscosity, as intended. Molecular

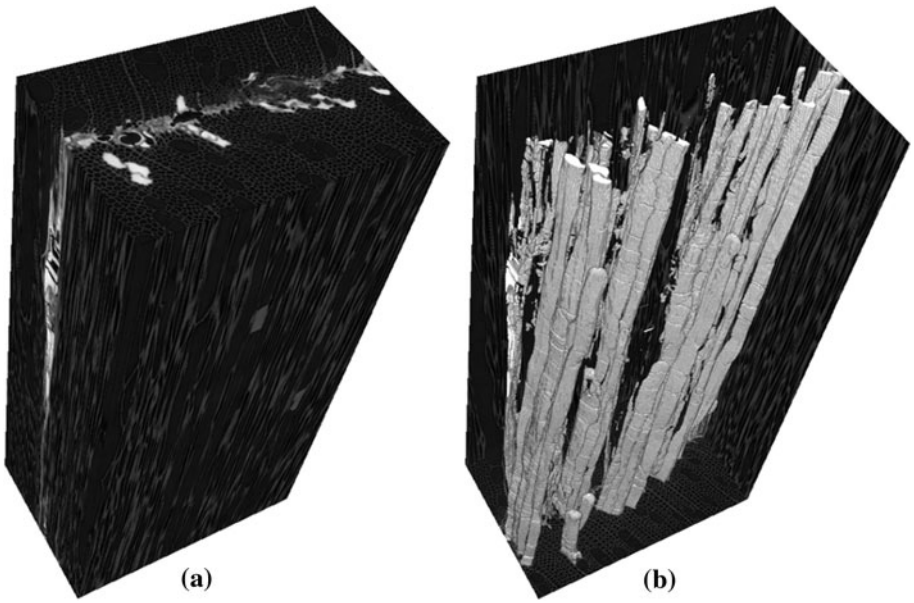

Fig. 2 XCT sub-volume (1.71 mm^3) virtually excised from the same HP, IPF2 specimen in Fig. 1e. **a** Solid 3D volume; **b** segmented, adhesive phase not including the wood material occupying the same internal space

Table 2 Adhesive material properties

Adhesive	Solids (%)	Powder density (g/cm^3)	Viscosity (mPa s)	Molecular weight			Cured resin tag concentration	
				Mn	Mw	PDI	Calculated (wt%)	Measured (wt%)
Control PF	43.2	1.43 (0.06)	600	3110	5920	1.90	–	–
BrPF	43.8	1.28 (0.06)	700	9180	16570	1.81	3.3	3.2
IPF1	44.0	1.57 (0.03)	515	14420	16360	1.13	12.1	12.2
IPF2	44.1	2.24 (0.06)	600	11800	22380	1.90	41.1	39.5 (0.2)
RbPF	47.0	1.3	750	1987	–	–	25.7	–

Molecular weight data include number average (Mn), weight average (Mw), and PDI (Mw:Mn). Standard deviation in parentheses ($n = 3$). BrPF and IPF NAA results are from a single replicate. RbPF results were adopted from another report [34]; RbPF density was estimated

weight increased with tag mass and quantity; however, each system had a similar polydispersity index (PDI), or ratio between weight average and number average molecular weights. IPF1 was the only exception, with slightly lower viscosity and PDI; its viscosity was expected to advance slightly between formulation and bonding. Curiously, BrPF had a noticeably reduced powder density than the control PF. Perhaps the *meta*-Br presence resulted in the formation of more linear polymer chains with lower potential cross-linking than the unsubstituted PF morphologies; in turn, this may have reduced the polymer packing efficiency upon resin cure. The higher GPC Mark–Houwink coefficients of the BrPF and IPF resins relative to the control lend credence to this view. The added void-volume may have offset the added mass from the heavier Br atoms, which were, after all, only present at 3.3 wt% in that system. Similar, polymer morphologies likely formed in the IPF1 and IPF2 resins, though the higher tag concentrations and masses were able to overcome any excess void-volume effects, and thus increase the overall cured density in these systems. In each resin, the calculated and measured concentrations agreed very closely, indicating that little to no tag material was liberated during formulation or cure.

Adhesive X-ray attenuation

X-ray absorption contrast depends on the relative difference in linear attenuation coefficient, μ, between neighboring materials; in turn, μ depends on material density and molecular formula [22]. To better understand why the RbPF system yielded good contrast, and to explain the results of the presented experimental resins, theoretical attenuation length was determined for each adhesive [40]. Attenuation length describes the depth an incident photon will penetrate into a material before its probability of being absorbed or scattered becomes $1/e$; μ is the inverse of attenuation length with units of reciprocal distance [22]. Theoretical attenuation lengths were calculated for the various materials in the XCT wood-composite specimens;

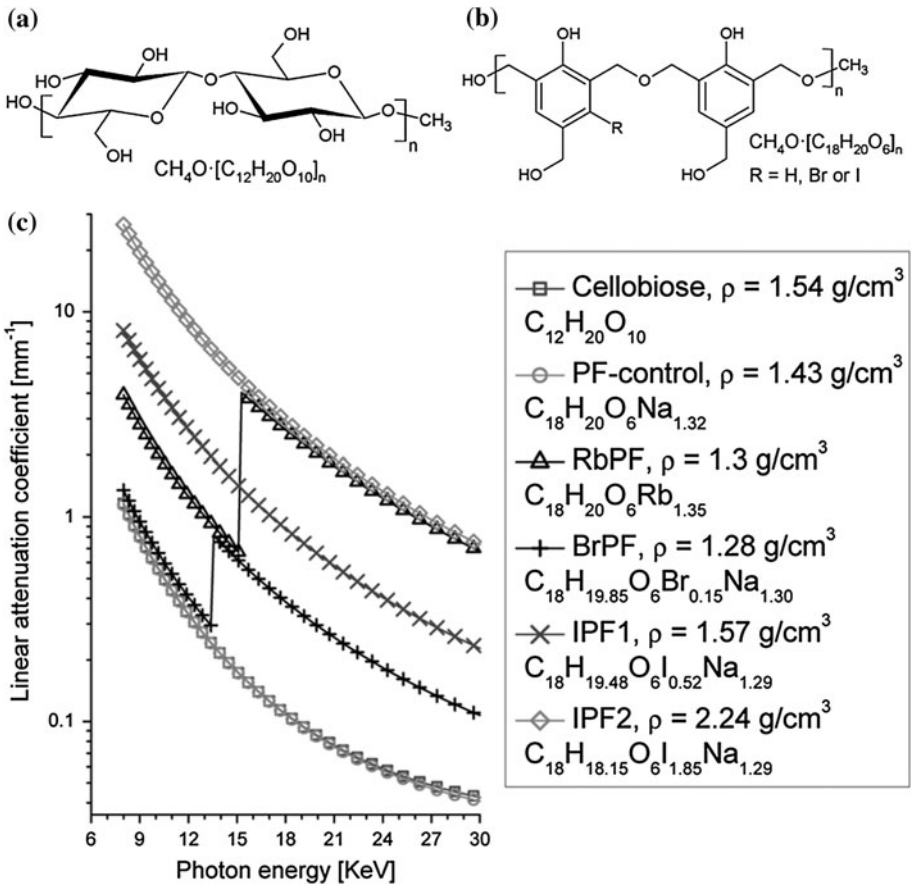

Fig. 3 Repeat units and molecular formulae for **a** cellobiose and **b** cured resol-PF adhesive polymers used to calculate theoretical attenuation coefficients for each material as a function of beam energy **c**; *plot key* indicates specific molecular formulae and density values used for each attenuation prediction

the observed differences in the theoretical μ values were expected to correlate with and elucidate the observed gray-scale contrasts. Cellobiose was chosen to represent wood cell-wall polymers, and was assigned a density equal to that of the cell-wall substance, approximately 1.54 g/cm^3. Figure 3a shows a representative cellobiose repeat unit. Cured adhesive formulae were calculated using the known formulation reactants and quantities, the measured solids content, and a theoretical PF dimer repeat unit. Figure 3b shows two phenol units which were first fully methylolated at the *para*- and *ortho*-positions, then polymerized linearly via a dimethylene ether linkage, common for resol-type PF adhesives at synthesis temperatures below 150 °C [35, 41, 42]. While it is likely that different morphologies also formed during polymerization and cure, this structure was assumed a good approximation for the attenuation calculation. IPF2 provided an opportunity to check this assumption, as each phenol unit should have exactly one iodine substituent. Accordingly, the IPF2 molecular formula based on the provided structure should have an iodine stoichiometric coefficient of two. The calculated iodine coefficient was 1.85, which was determined sufficiently close to mass balance considering that the calculation contained additional variability in the solids and reagent quantities.

Figure 3c is a plot of log attenuation coefficient as a function of beam energy; the figure key provides the density and molecular formula used for each material in the calculation [40]. Cellobiose attenuation closely matched theoretical wood results presented elsewhere [13]. It is clear that with similar molecular formulae and density there is no discernible difference in attenuation between the control PF and cellobiose within the provided photon energy range. As a result, XCT reconstructions of wood-composites bonded with control PF adhesives failed to provide enough image contrast for material segmentation (Fig. 1a, bondline). Just above the Rb *k*-shell electron binding energy (*k*-edge = 15.3 keV), the calculated RbPF attenuation coefficient is 24 times greater than that for cellobiose. RbPF yielded sufficient image contrast (Fig. 1b, bondline) in this energy range, yet quantitative segmentation suffered from tag mobility complications [34]. BrPF, scanned just above the Br *k*-edge (13.7 keV), yielded a theoretical attenuation coefficient only three and a half times more than cellobiose; this clearly was not enough for sufficient contrast (Fig. 1c, bottom). The predicted IPF1 attenuation is about seven times greater than that for cellobiose within the range studied; however, IPF1 specimens were scanned above the I *k*-edge (33.2 keV), which was beyond the attenuation calculation range [40]. Nevertheless,

a sharp increase in attenuation was expected above the *k*-edge, similar to the Br and Rb species. However, the increased energy also significantly reduced the cellobiose attenuation, which increased image noise.

Scintillator detectors assign photon intensities to specific gray levels ranging from pure black to pure white, with a floating point value. Quantitative phase segmentation with simple gray-scale threshold operations requires clearly defined valleys between material peaks; furthermore, segmentation confidence increases with decreasing peak overlap. The bondline histograms in Fig. 1 illustrate this concept. Composite specimen b exhibits two clear peaks, which can be segmented with a threshold centered in the valley separating them; for specimen e, three material phases could be quantitatively segmented as there are two clear valleys (Fig. 1). Image processing procedures, such as edge-preserving median filters, can further decrease phase overlap and improve segmentation confidence [12, 19, 20, 43]; however, some initial contrast is still necessary. Wood-based composites contain three separate material phases—air, wood, and adhesive; an optimal histogram for quantitative segmentation would thus consist of three isolated peaks distributed along the gray-scale range, as observed in Fig. 1e. Peak height represents pixel count for a particular gray value, while peak breadth relates to how confidently one can assign a peak to a particular material. Broader peaks represent low signal-to-noise levels and/or overlaps in material gray values. The tallest peak in each histogram represents air; the brighter peak (high gray-scale value), or shoulder when there is little contrast, immediately to the right of the air peak represents wood cell-walls. The darker peak (low gray-scale value), or shoulder, left of the air peak is an artifact caused by large differences in density and refractive index at the interface of dissimilar materials [10, 34, 44]. With a fixed gray-scale range, simply maximizing the attenuation difference between any two phases could reduce the achievable contrast for the third. For example, Fig. 1d shows the greatest overlap between the air and wood peaks, and these specimens were scanned at the highest energy.

X-ray radiographs of control PF and IPF1 adhesive powders were collected to determine if absorption contrast could be enhanced with increasing wt% I, even below the iodine *k*-edge. Figure 4 compares the mean gray-scale pixel intensity from regions containing air-space and ground resin in each projection image. Note that the response variable in this figure is transmission intensity, which is opposite from XCT gray-scale intensity. In radiographic projections, high pixel intensities correspond with high photon transmission through the material (i.e., low absorption); with XCT high pixel intensities related to high attenuation (i.e., low transmission). Air intensity was uniform in each projection, while adhesive transmission

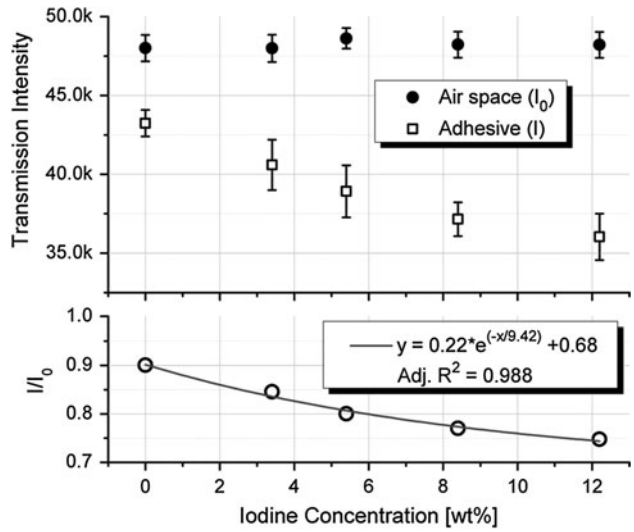

wt% I	0.0	3.4	5.4	8.4	12.2
ρ_{bulk} [g/cm³]	0.71	0.61	0.59	0.58	0.54
v_a	46.0	57.5	56.8	61.1	63.4

Fig. 4 (*Top*) Mean X-ray transmission (*gray*-scale) intensity through air and adhesive powder with increasing wt% iodine, *error bars* indicate ±1 standard deviation; (*bottom*) mean intensity ratio, I/I_0, and fitted regression line; measured wt% *I*, apparent densities and void-volume fractions are also provided

intensity decreased significantly from zero to 12.2 wt% I. Bulk, or apparent, density (ρ_{bulk}) was checked as a confounding factor since X-ray attenuation is influenced by density and composition [22]. The void-volume fraction (v_a) in the powder column is inversely proportional to ρ_{bulk}. Despite cured IPF1 being denser than control PF, ρ_{bulk} and v_a did not correlate with the observed intensity behavior (Fig. 4).

In both air-space and adhesive-filled regions, the transmitted X-rays passed through both container walls and the internal material. The relationship between adhesive intensity (I) and airspace intensity (I_0) was expected to follow the Beer–Lambert attenuation law, and an exponential fit to the ratio data showed a high adjusted R^2 of 0.988. The significance of the relationship showed that even below the iodine *k*-edge, and independent of bulk density, increasing iodine concentration would further reduce transmission intensity, resulting in greater XCT contrast.

IPF2 was prepared based on the results from both BrPF and IPF1. *Meta*-iodophenol made up the entire phenol component in IPF2, to maximize the achievable iodine concentration with the presented method and ensure that all resin polymers were substituted to the same degree, regardless of chain length. Cured IPF2 contained 39.9 wt% I, and had a density of 2.24 g/cm^3 (Table 2). Accordingly, IPF2 showed the highest theoretical attenuation of all adhesives including RbPF (Fig. 3c). Subsequent XCT data,

collected below the iodine *k*-edge, yielded significantly enhanced adhesive contrast. The bondline image in Fig. 1e shows dark void spaces in empty lumens, light-gray cell-walls, and bright adhesive at the bond interface and in several vessels; these phases correspond to the three primary peaks in the IPF2 bondline histogram. Also, the IPF2 adhesive gray value is more consistent than the other systems, as evident by the clear, rightmost peak in the bondline histogram (Fig. 1e). This observation is intuitive because all IPF2 polymer chains contained the same degree of iodine substitution. In Fig. 1b, RbPF appears less consistent; the brightest regions likely indicate higher Rb concentrations [34]. Consequently, the RbPF bondline histogram shows no clear distinction between wood and adhesive peaks; rather, they form one broad peak which extends farther along the gray-scale range than the shoulder in the wood-only histogram. As was the case, RbPF could not be segmented. The IPF2 system, however, was segmented (Fig. 2) with gray-scale thresholds in the valleys between each peak.

The above results indicate that density, molecular formula, tag uniformity, and signal-to-noise ratio all impact adhesive X-ray contrast. Wood and adhesives are complex, organic systems with similar density; X-ray absorption contrast between the two materials requires ample difference in attenuation coefficients. Perhaps, an adhesive consisting entirely of *meta*-bromophenol would achieve similar results as IPF2 if it were scanned just above the Br *k*-edge; however, its density would likely be lower than IPF2. Similarly, one might argue that contrast might be even greater for IPF2 if it were imaged above the I *k*-edge; yet, this would increase image noise since beam attenuation in wood is drastically decreased at such high beam energies.

Tag mobility assessment

Quantitative segmentation of a tagged adhesive requires the contrast agent to remain attached and uniformly distributed along the polymers throughout both the formulation and bonding processes. Initially, there was concern that the Br and I tags, attached at the *meta*-position of the phenol reactants, might be released from the aromatic rings when exposed to the high temperature and pH reaction environments during adhesive cook. However, IC results showed no free bromide or iodide ions in any of the experimental adhesives following formulation. Composite specimens were bonded at still higher temperatures than formulation. NAA results confirmed that resin powders contained the same tag concentrations as predicted (Table 2); yet, it was unclear whether the Br and I were, in fact, still attached to the cured PF polymers. Fluorescent micrographs and EDS elemental maps were used to determine if observed adhesive locations corresponded with tag spectra. Figure 5 compares the FM and EDS images from the same surfaces of specimens bonded with each resin. In each FM image, dark PF adhesive shows clear contrast to surrounding, light-colored cells. In EDS images, the oxygen elemental signal, shown in red, most clearly represented the wood structure, as the embedding epoxy had a lower oxygen concentration than the surrounding cell-walls. Tag element maps, shown in green, are overlain on the oxygen maps. EDS spectra include the cumulative detected fluorescent counts from 64 scans for each element of interest. Raw images exhibited a uniform level of background noise from low-intensity pixels only detected in a single or few scans; however, this was easily removed with simple image processing.

Figure 5b shows Rb contamination in cell-walls far from the RbPF specimen bondline and around cell lumens void of adhesive; this supports earlier evidence that the Rb ions moved independent of the adhesive polymers [15, 34]. The EDS images of BrPF, IPF1, and IPF2 (Fig. 4d, f, and h, respectively) show tag signals directly corresponding with the adhesive locations in the matching FM images. For BrPF and IPF1, only a portion of the phenol reactants were substituted. Tag concentration in these systems were likely heterogeneous across different polymer molecular weights, and thus polymer mobility was effected; this might explain the observed non-uniformity in tag-signal intensity. However, iodine intensity in IPF2 appears consistent at all adhesive locations. Additionally, semi-quantitative point spectra of the Br- and I-tagged composite specimens showed that there were no measurable traces of tags on cell-wall edges far from the bondline and not in contact with adhesive.

Rb ions were included as an alkaline catalyst during the RbPF adhesive formulation [15]; the conventional catalyst system, NaOH was used in formulation of the BrPF and IPF resins. Figure 5i shows the Na elemental map for the IPF2 specimen. As with Rb (Fig. 5b), the Na signal intensity appears non-uniform in the bondline region, and Na ions migrated far from the bond interface. However, unlike the Rb ions, sodium appeared indiscriminately in both cell-walls and epoxy-filled lumens. This is not surprising as Na is much smaller and more reactive than Rb, affording it greater mobility. Na ions distributed throughout the wood cells after adhesive cure were likely remobilized by the liquid epoxy embedding media before it hardened. Several studies have shown similar migration and agglomeration behavior for ions or metal particles dispersed in liquids designed to penetrate wood structures [9, 13, 23, 24, 45, 46]. Often wood's heterogeneous chemical and anatomical structures magnify these separation effects. Charged ions may be preferentially absorbed into different cell-wall layers, and micro- or nano-sized

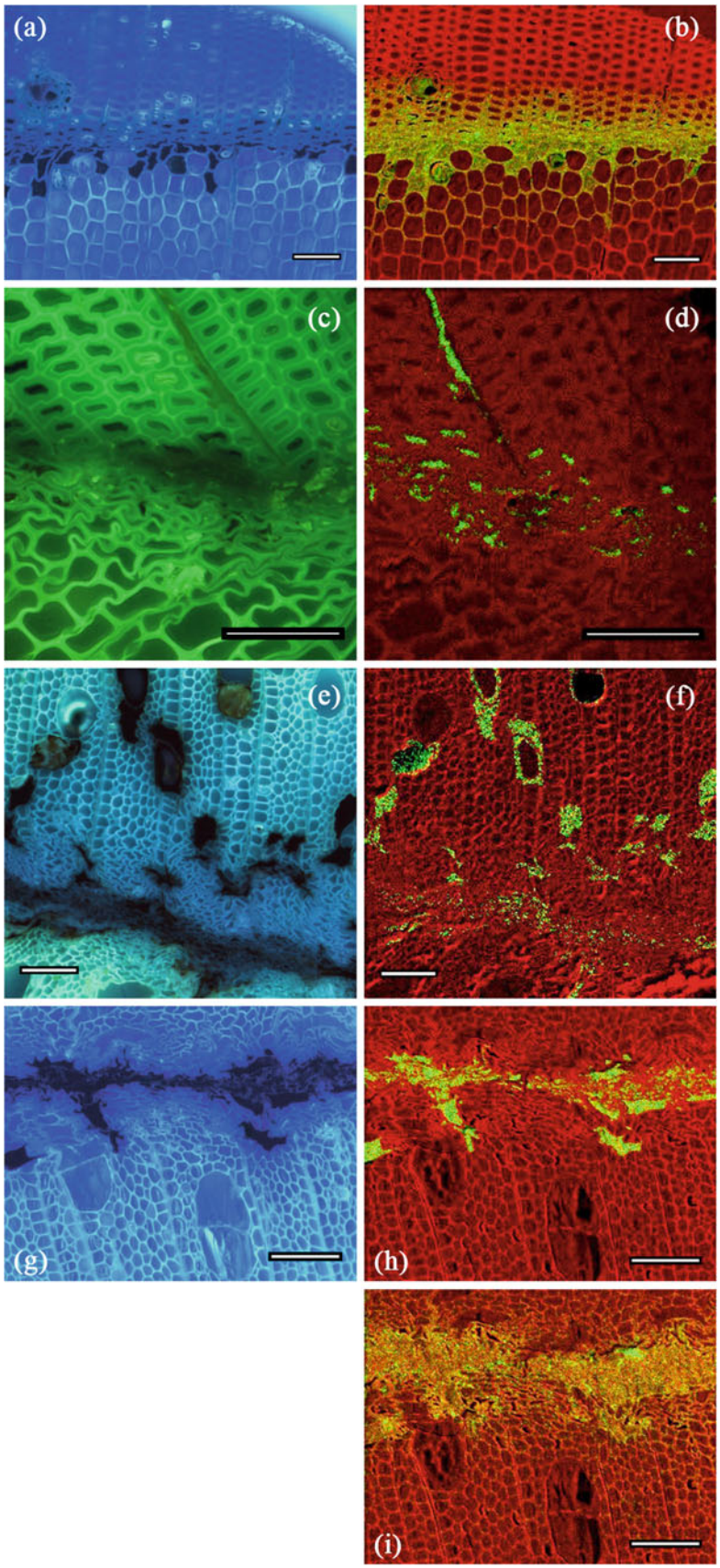

Fig. 5 FM images (*left*) and EDS elemental maps (*right*) of the same specimen surface for composites bonded with RbPF (**a** and **b**, DF), BrPF (**c** and **d**, SYP), IPF1 (**e** and **f**, HP), and IPF2 (**g**–**i**, HP). BrPF FM image (**c**) acquired with blue filter set and (**a**, **e**, and **g**) acquired with UV filter set. EDS *red phase* represents oxygen signal and *green* indicates tag element of interest: Rb (**b**), Br (**d**), I (**f** and **h**), and Na (**i**). *Scale bars* = 100 μm

metallic particles can often be size-excluded from penetration by small pit structures [45, 46]. Therefore, if contrast agents are required to quantify the penetration behavior of an adhesive or solution into wood structures, consideration must be given to chemical or physical phase separation.

The collective IC and EDS results indicate that the halogen substituents remained attached to the phenol reactants throughout formulation and bonding. Furthermore, the IPF2 tag concentration appeared uniform across the polymer molecular weight distribution, since it consisted entirely of *meta*-iodophenol; this observation is consistent with the uniform XCT gray-scale intensity in Fig. 1e. It is true that one would not expect a PF resin prepared with a substituted phenol to polymerize in the same manner as one containing only phenol. However, the goal of this work was to develop an adhesive system which could be confidently segmented from wood-composite XCT data. The BrPF and IPF adhesives presented here were formulated according to one particular recipe. This of course could be adjusted for different desired molecular weight distributions, viscosities, solid contents, or cross-linking potentials, all of which in turn would affect adhesive penetration and performance behavior.

Conclusions

A resol-type, PF adhesive formulated with *meta*-iodophenol yielded sufficient and consistent micro-XCT image contrast in bonded wood-composites. Air, wood, and adhesive phases could all be segmented from reconstructed 3D datasets with simple histogram thresholds centered between the three material gray-scale peaks. Preliminary adhesives containing lower concentrations of iodine or bromine were also presented and compared with a control and rubidium-labeled adhesive. X-ray absorption contrast improved with increasing tag mass and concentration and cured adhesive density; however, image quality and segmentation confidence suffered at high beam energies when signal-to-noise levels were low. X-ray results for wood and adhesives agreed with theoretical attenuation behavior predicted for each material as a function of beam energy. Tag efficacy and mobility were also accessed with multiple chemical and visual analyses including ion chromatography, NAA, fluorescent microscopy, and energy-dispersive spectrometry. The iodine and bromine tags, originally covalently bonded to the formulation reactants, remained associated with the liquid and cured adhesive polymers. Sodium and rubidium, which were merely mixed into the liquid adhesives as polymerization catalysts, retained high mobility, and migrated independent of the adhesive polymers during bonding. The presented formulation could be modified to achieve different viscosities, solid contents, or molecular weight distributions, which would in turn influence penetration behavior and joint performance. The afforded X-ray tomography contrast and segmentation confidence with these tagged adhesives can help improve fundamental understanding of wood adhesion and the role of adhesive penetration.

Acknowledgements Use of the Advanced Photon Source was supported by the U.S. Department of Energy, Office of Science, Office of Basic Energy Sciences, under Contract No. DE-AC02-06CH11357. The Advanced Light Source is supported by the Director, Office of Science, Office of Basic Energy Sciences, of the U.S. Department of Energy under Contract No. DE-AC02-05CH11231. Financial support was provided by the Wood-Based Composites Center, a National Science Foundation Industry/University Cooperative Research Center. Resin formulation and technical assistance were provided by Arclin, in Springfield, Oregon.

References

1. Pocius AV (1997) Adhesion and adhesives technology: an introduction. Hanser/Gardner, Munich
2. Schultz J, Nardin M (1994) In: Pizzi A, Mittal KL (eds) Handbook of adhesive technology. Marcel Dekker, New York, p 19
3. Ebewele RO, River BH, Koutsky JA (1982) J Adhes 14(3–4):189
4. White MS (1977) Wood Sci 10(1):6
5. Frazier CE, Ni JW (1998) Int J Adhes Adhes 18(2):81
6. Kamke FA, Lee JN (2007) Wood Fiber Sci 39(2):205
7. Banhart J (2008) In: Banhart J (ed) Advanced tomographic methods in materials research and engineering. Oxford University Press, Oxford, p 107
8. Banhart J (2008) In: Banhart J (ed) Advanced tomographic methods in materials research and engineering. Oxford University Press, Oxford, p 3
9. De Vetter L, Cnudde V, Masschaele B, Jacobs PJS, Van Acker J (2006) Mater Charact 56(1):39. doi:10.1016/j.matchar.2005.09.007
10. Haibel A (2008) In: Banhart J (ed) Advanced tomographic methods in materials research and engineering. Oxford University Press, Oxford, p 141
11. Hass P, Wittel F, Mendoza M, Herrmann H, Niemz P (2011) Wood Sci Technol 46(1–3):1. doi:10.1007/s00226-011-0410-6
12. Hass P, Wittel FK, McDonald SA, Marone F, Stampanoni M, Herrmann HJ, Niemz P (2010) Holzforschung 64(5):639. doi:10.1515/hf.2010.103
13. Mannes D, Marone F, Lehmann E, Stampanoni M, Niemz P (2010) Wood Sci Technol 44(1):67. doi:10.1007/s00226-009-0257-2
14. Mannes D, Niemz P, Lehmann E (2009) Wood Res 54(3):33
15. Modzel G, Kamke FA, De Carlo F (2010) Wood Sci Technol 45(1):147. doi:10.1007/100226-010-0304-z
16. Evans PD, Morrison O, Senden TJ, Vollmer S, Roberts RJ, Limaye A, Arns CH, Averdunk H, Lowe A, Knackstedt MA (2010) Int J Adhes Adhes 30(8):754. doi:10.1016/j.ijadhadh.2010.08.001
17. Bucur V (2003) Meas Sci Technol 14(12):R91
18. Forsberg F, Sjodahl M, Mooser R, Hack E, Wyss P (2010) Strain 46(1):47
19. Mayo SC, Chen F, Evans R (2010) J Struct Biol 171(2):182. doi:10.1016/j.jsb.2010.04.001
20. Trtik P, Dual J, Keunecke D, Mannes D, Niemz P, Stähli P, Kaestner A, Groso A, Stampanoni M (2007) J Struct Biol 159(1):46. doi:10.1016/j.jsb.2007.02.003

21. Wildenschild D, Hopmans JW, Vaz CMP, Rivers ML, Rikard D, Christensen BSB (2002) J Hydrol 267(3–4):285. doi:10.1016/s0022-1694(02)00157-9
22. Ketcham RA, Carlson WD (2001) Comput Geosci 27(4):381. doi:10.1016/s0098-3004(00)00116-3
23. Walther T, Thoemen H (2009) Holzforschung 63(5):581. doi:10.1515/hf.2009.093
24. Wang Y, Muszyński L, Simonsen J (2007) Holzforschung 61(6):723. doi:10.1515/hf.2007.117
25. ASTM-D-4426 (2006) ASTM D 4426-01. ASTM International, West Conshohocken
26. ASTM-D-5965 (2007) ASTM B 5965-02. ASTM International, West Conshohocken
27. Minc LD (2008) Neutron activation analysis. Encyclopedia of archaeology. Academic, New York
28. Schindelin J, Arganda-Carreras I, Frise E, Kaynig V, Longair M, Pietzsch T, Preibisch S, Rueden C, Saalfeld S, Schmid B (2012) Nat Methods 9(7):676
29. Rasband WS (1997–2012) ImageJ. U.S. National Institutes of Health, Bethesda, Maryland. http://imagej.nih.gov/ij/
30. Spurr AR (1969) J Ultrastruct Res 26:31
31. Ellis E (2006) Microsc Today 14(4):32
32. Davidson MW, Abramowitz M (2002) In: Hornak J (ed) Encyclopedia of imaging science and technology. Wiley, New York. doi:10.1002/0471443395.img074
33. Dowd BA, Campbell GH, Marr RB, Nagarkar VV, Tipnis SV, Axe L, Siddons DP (1999) In: Proceedings of the SIPE. pp 224–236. doi:10.1117/12.363725
34. Modzel G (2009) Dissertation, Oregon State University, Corvallis, OR
35. Pizzi A (2003) In: Pizzi A, Mittal KL (eds) Handbook of adhesive technology, 2nd edn. Marcel Dekker, New York
36. Sellers T (1994) In: Pizzi A, Mittal KL (eds) Handbook of adhesive technology. Marcel Dekker, New York, p 599
37. Smith L, Côté W (1971) Wood Fiber Sci 3(1):56
38. White MS, Ifju G, Johnson JA (1977) For Prod J 27(7):3
39. Umemura K, Takahashi A, Kawai S (1998) J Wood Sci 44(3):204
40. Henke BL, Gullikson EM, Davis JC (1993) At Data Nucl Data Tables 54(2):181
41. Frihart CR (2005) In: Rowell RM (ed) Handbook of wood chemistry and wood composites. Taylor & Francis, New York
42. Park B-D, Riedl B, Yoon Soo K, So WT (2002) J Appl Polym Sci 83(7):1415. doi:10.1002/app.2302
43. Standfest G, Kutnar A, Plank B, Petutschnigg A, Kamke F, Dunky M (2012) Wood Sci Technol 47(1):121. doi:10.1007/s00226-012-0496-5
44. Betz O, Wegst U, Weide D, Heethoff M, Helfen L, Lee WK, Cloetens P (2007) J Microsc 227(1):51
45. Matsunaga H, Kiguchi M, Evans PD (2009) J Nanopart Res 11(5):1087. doi:10.1007/s11051-008-9512-y
46. Matsunaga H, Matsumura J, Oda K (2004) IAWA J 25(1):79